Available online at www.sciencedirect.com
ScienceDirect
Journal of Power Sources 178 (2008) 207–222
JOURNAL OF POWER SOURCES
www.elsevier.com/locate/jpowsour

Parameterization and prediction of temporal fuel cell voltage behavior during flooding and drying conditions

Denise A. McKay [a,*], Jason B. Siegel [b], William Ott [c,1], Anna G. Stefanopoulou [c]

[a] Department of Civil and Environmental Engineering, University of Michigan, Ann Arbor, MI, USA
[b] Department of Electrical Engineering and Computer Science, University of Michigan, Ann Arbor, MI, USA
[c] Department of Mechanical Engineering, University of Michigan, Ann Arbor, MI, USA

Received 11 September 2007; received in revised form 3 December 2007; accepted 5 December 2007
Available online 31 January 2008

Abstract

This paper describes a simple isothermal two-phase flow dynamic model that predicts the experimentally observed temporal behavior of a proton exchange membrane fuel cell stack. This model is intended for use in embedded real time control where computational simplicity is of critical importance. A reproducible methodology is presented to experimentally identify six (6) tunable physical parameters based on the estimation of the cell voltage, the water vapor transport through the membrane and the accumulation of liquid water in the gas channels. The model equations allow temporal calculation of the species concentrations across the gas diffusion layers, the vapor transport across the membrane, and the degree of flooding within the cell structure. The notion of apparent current density then relates this flooding phenomena to cell performance through a reduction in the cell active area as liquid water accumulates. Despite the oversimplification of many complex phenomena, this model provides a useful tool for predicting the resulting decay in cell voltage over time only after it has been tuned with experimental data. The calibrated model and tuning procedure is demonstrated with a 1.4 kW (24 cell, 300 cm^2) stack, using pressure regulated pure hydrogen supplied to a dead-ended anode, under a range of operating conditions typical for multi-cell stacks.

Keywords: PEM fuel cells; Anode flooding; PDE modeling; Transient dynamics; Model calibration; Parameter identification

1. Introduction

The management of water is critical for optimizing performance of a polymer electrolyte membrane fuel cell (PEMFC) stack. Because the ionic conductivity of the membrane is dependent upon its water content [1], a balance must be struck between reactant (hydrogen and oxygen) delivery and water supply and removal. Depending upon the operating conditions of the PEMFC stack, the flow patterns in the anode and cathode channels, and the design of the anode gas delivery system (dead-ended or flow through), this liquid water can accumulate within the gas diffusion layers (GDLs) and channels [2–5], as shown in Fig. 1. Whether obstructing reactant flow or reducing the number of active catalyst sites, the impact of flooding is a reduction in the power output of the fuel cell stack, seen by a decrease in cell voltage [6]. Thus, a real-time estimation of the degree of flooding within the cell structure and its impact on the cell electrical output with standard, cheap, and reliable sensors is critical for active water management. Moreover, a low order control-oriented model must be derived for further considering such issues as identifiability, observability, and controllability.

To gain a better understanding of reactant and water transport within the GDL and catalyst layers, many CFD models have been developed to approximate the two- or three-dimensional flow of hydrogen, air, and water at steady-state within the cell structure [7–12]. Using experimental steady-state polarization (voltage versus current) data for parameter identification, Guo et al. [13] and Carnes and Djilali [14] investigated the sensitivity of the cell performance to the identified parameters. Further, using a model to simulate polarization data with a given set of parameters, constrained quadratic programming was then used to identify these given parameters [15]

* Corresponding author. Tel.: +1 7347644272.
E-mail address: dmckay@umich.edu (D.A. McKay).
[1] Currently with the Southwest Research Institute, USA.

0378-7753/$ – see front matter © 2007 Elsevier B.V. All rights reserved.
doi:10.1016/j.jpowsour.2007.12.031

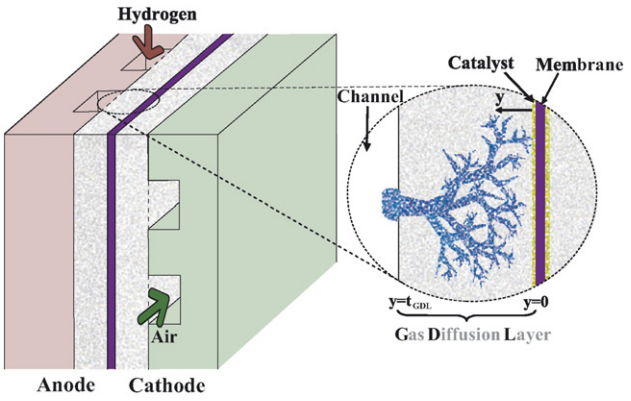

Fig. 1. Schematic of capillary flow of liquid water through the gas diffusion layers.

and address parameter identifiability and uniqueness issues [16].

While these models are ideal for investigating transport phenomena with two phase flow and spatial gradients, examining parameter sensitivity, or the influence of material properties on cell performance, experimental validation of these models, often completed by comparing measured to estimated polarization curves, is still lacking. A few publications with steady-state validation efforts (i) point to a mismatch between model prediction and spatially resolved experimental data [17] indicating that different spatial distributions can correspond to a similar averaged polarization curve [16,17], and (ii) achieve good prediction of steady-state and spatially resolved current density measurements after tuning parameters to several orders of magnitude of their theoretical values [18].

Although steady-state polarization measurements do not offer a conclusive data set for model validation, the transient polarization response provides useful data for model validation especially during unsteady operation such as flooding [19,20]. Several transient models have been reported to illicit the relationship between critical material properties and operating conditions on the dynamic fuel cell response [21–25], however few have been validated against transient experimental data and are of sufficient complexity for implementation in real time control applications.

Control-oriented transient models have been developed to account for the formation of liquid water within the gas channels [26] or within both the channels and the GDL [27], however they do not relate the effect of flooding to decreased cell potential, a key indication of how flooding impacts cell performance. A relationship between flooding and cell performance was introduced in Ref. [20], appearing later in Ref. [28], using the notion of apparent current density to relate the accumulation of liquid water in the gas channels to a reduction in the cell active area, in turn increasing the cell current density and lowering cell voltage. Although the apparent current density calculation based on the water accumulation in the channels approximates the cell voltage behavior well during a range of transient and steady conditions the stack typically operates in, more experimental evidence and justification of this simplification is needed and is underway in our laboratory.

In this paper, we present a low order model of the liquid water and gas dynamics within the GDL to simulate both the effects of reactant starvation and flooding. We focus on the one-dimensional dynamics through the GDL thickness, assuming invariant two-dimensional properties in the plane parallel to the membrane, lumped volume manifold filling dynamics for the gas channels, and lumped parameter characteristics for the membrane. Lumping the GDL and channel into a single volume, Hernandez et al. [29] experimentally validated their model for a flow-through anode with no gas dynamics. Lumping the GDL volume was also pursued in Ref. [28] and validated against experimental data for a Ballard® NEXA ™ system. Note that [28] nearly doubled the number of experimentally identified parameters from the work originally presented in Ref. [20] and used here.

In this paper we extend and test the validity of [20] to a wider range of current densities (0–0.3 A cm^{-2}), temperature (45–65 °C) and air stoichiometries (150–300%). These conditions are tested while the stack operates mostly under full hydrogen utilization with intermittent and short high hydrogen flow conditions associated with dead-ended anode operation. It is shown that our model predicts both the fast voltage dynamics during step changes in current (the gas dynamics) and the slow voltage behavior while liquid water is accumulating in the GDL and gas channels (water dynamics), whereas [28] only predicts the slow voltage dynamics well. Hence, the model presented here can be used for estimation and control of fuel cell water and gas dynamics. It is important to note that the fuel cell model presented here is not novel except in relating cell flooding to performance. The unique contribution lies in applying this simple isothermal model to well approximate the dynamic fuel cell response under a range of operating conditions by leveraging standard off-the-shelf sensors and actuators.

This paper is organized by first presenting the experimental hardware in Section 2 followed by the model of gas and water dynamics in Section 3. The applied boundary conditions at the gas channels and membrane surface are then presented in Section 4. The impact of the liquid water on cell voltage is modeled in Section 5. The parameter identification methodology is presented in Section 6. Finally, the model calibration and validation results are shown in in Sections 7 and 8. A list of the model parameters is given in Appendix A.

2. Experimental hardware

Experimental results are collected from a 24-cell PEMFC stack which can deliver 1.4 kW continuous power, capable of peaking to 2.5 kW. The cell membranes are comprised of GORE ™PRIMEA® Series 5620 membrane electrode assemblies (MEAs). The MEAs utilize 35 μm thick membranes with 0.4 mg cm^{-2} and 0.6 mg cm^{-2} Pt/C on the anode and cathode, respectively, with a surface area of approximately 300 cm^2. The GDL material, which distributes gas from the flow fields to the active area of the membrane, consists of double-sided, hydrophobic, version 3 ETek™ ELATs® with a thickness of 0.43 mm. The flow fields are comprised of machined graphite plates with gas channels that are approximately 1 mm wide and

1 mm deep. The flow pattern consists of semi-serpentine passages on the cathode (30 channels in parallel that are 16.0 cm in length with two 180° turns) and straight passages on the anode (90 channels in parallel that are 17.1 cm in length).

The experimental hardware, designed in collaboration with the Schatz Energy Research Center at Humboldt State University, is installed at the Fuel Cell Control Laboratory at the University of Michigan. A schematic of the major experimental components along with the measurement locations is depicted in Fig. 2. A computer controlled system coordinates air, hydrogen, cooling, and electrical subsystems to operate the PEMFC stack. Dry pure hydrogen is pressure regulated at the anode inlet to a desired setpoint. This pressure regulation system replenishes the hydrogen consumed in the chemical reaction. For the majority of the operational time, the hydrogen stream is dead-ended with no flow external to the anode. Using a purge solenoid valve, hydrogen is momentarily purged through the anode to remove water and inert gases. Humidified air (generated using a membrane-based internal humidifier) is mass flow controlled to a desired stoichiometric ratio. Deionized water is circulated through the system to remove heat produced due to the exothermic chemical reaction. A fan is used to thermostatically control (on–off) the stack outlet coolant to a desired temperature. Measurements of the dry gas mass flow rates supplied to the PEMFC stack are taken along with the temperature, pressure and relative humidity in the inlet and outlet manifolds.

Due to the lack of a practical means to directly measure the accumulation of liquid water within a multi-cell stack, consecutive anode purges and cathode surges (momentarily increasing the gas mass flow rates) were used to indicate the presence of liquid water in either the anode or cathode channels, as shown in Fig. 3. At approximately 240 s the cathode was surged, causing an increase in oxygen partial pressure and cell voltage. However, this momentary voltage increase is not sustained following the surge and the general voltage decay due to flooding in the anode persists. Following an anode purge, the voltage quickly improves and then gradually decays until the next anode purge event is initiated. It is important to note that this gradual decay in

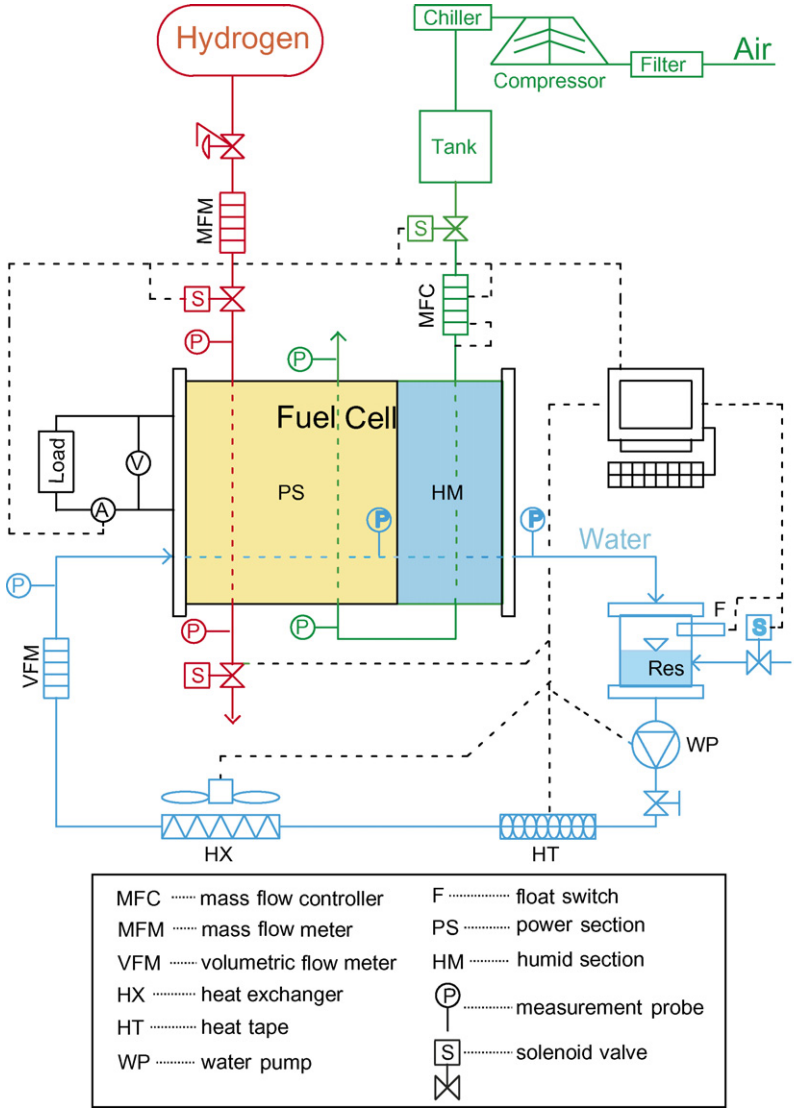

Fig. 2. Experimental hardware employed and measurement locations. This figure is modified from [52].

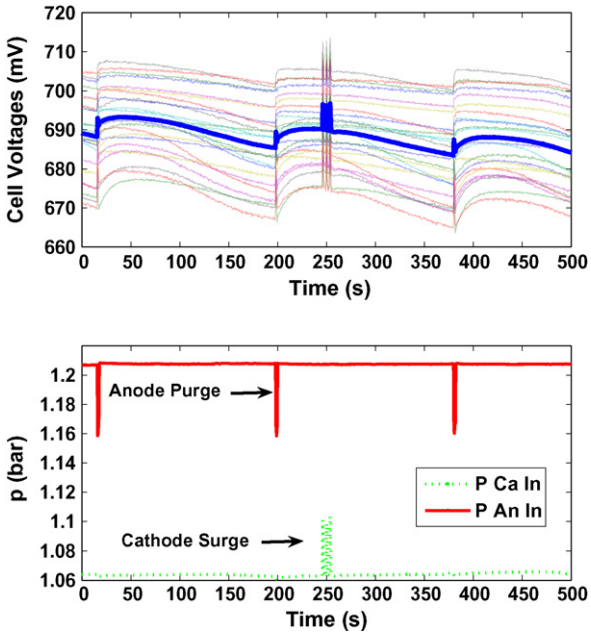

Fig. 3. Experimental data showing impact of anode purging and cathode surging on cell voltages at a constant nominal current density of 0.3 A cm^{-2}, and an operating temperature of $T = 65\,^{\circ}C$. The first subplot shows the 24 individual cell voltages in thin lines along with the average cell voltage with a thick line. The second subplot shows the anode and cathode inlet total pressures.

cell voltage could be attributed to the accumulation of nitrogen in the anode which would also be expelled during and anode purge event. However, during purge events a significant mass of liquid water can be visually detected leaving the anode. Thus, this work focuses on the impact of anode flooding on cell voltage and assumes nitrogen is not the culprit.

3. Modeling of gas and water dynamics

The model of the reactant and water dynamics is presented in the following sections, describing the capillary transport of liquid water and the diffusion of gases within the GDL, as well as the time varying boundary conditions at the membrane and gas channel interfaces. To approximate the spatial gradients, the gas diffusion layer was separated into discrete volumes using standard finite difference techniques.

The anode volume contains a mixture of hydrogen and water vapor, whereas the cathode volume contains a mixture of oxygen, nitrogen, and water vapor. The species concentrations in the channel are calculated based on the conservation of mass assuming the channel is homogeneous, lumped-parameter, and isothermal. Under load, we assume product water is formed in the vapor phase.

This product water vapor, combined with the water vapor supplied with the cathode gas stream, is exchanged between the anode and the cathode through the hydrophilic membrane. The protons, liberated at the anode, transport water to the cathode through electro-osmotic drag, while back diffusion transfers vapor due to a water vapor concentration gradient across the membrane. The net flux of vapor through the membrane depends on the relative magnitudes of these transport mechanisms. Although there are many efforts to experimentally quantify back diffusion [30–33], conflicting results suggest an empirically data-driven identification of water vapor diffusion might be a practical approach to this elusive subject. Constant parameters have been used to scale back diffusion models for PEMFCs with different membrane materials [27,34]. Using a similar methodology as [27], in this paper the membrane water transport algorithm employs a tunable parameter to scale the membrane water diffusion model in Ref. [31].

When the production or transport of water vapor overcomes the ability of the vapor to diffuse through the GDL to the channel, the vapor supersaturates and condenses. The condensed liquid water accumulates in the GDL until it has surpassed the immobile saturation limit at which point capillary flow will carry the liquid water to an area of lower capillary pressure (the GDL–channel interface). Liquid water in the GDL occupies the pore space, reducing the diffusion of the reactant gases. However, we have found that the reduction of the reactant concentrations due to the changes in the gas diffusivity alone is not significant enough to degrade the voltage by the magnitude experimentally observed. Similar observations lead to the consideration of the reactant diffusion in the catalyst layer [35].

We follow here a different approach and instead of adding the catalyst layer complexity to the model, we consider the effects of flooding on the area available for diffusion. The water (in liquid and vapor phase) that wicks out of the hydrophobic GDL to the channel ultimately obstructs the area that reactants can diffuse through. This effect is not easily modeled because the GDL surface roughness makes it difficult to predict how much GDL surface area is blocked by a given volume of liquid water. For this reason, we assume the liquid water at the GDL–channel interface forms a layer of uniform thickness. This water layer spreads across the surface of the GDL as the volume of liquid water in the channel increases, thus reducing the surface area, which increases the calculated current density, in turn lowering the cell voltage at a fixed total stack current. In this model the thickness of the water layer is an experimentally tuned parameter.

The estimation of the average cell voltage is a function of the reactant concentrations at the surface of the membrane, the membrane water content, temperature, and the calculated current density based on the reduced active area, which in turn is a function of liquid water present in the gas channel. There are four experimentally tunable voltage parameters which are determined using linear least squares for a given set of membrane diffusion and water thickness parameters. By comparing the average measured cell voltage to the model prediction, these parameters can be re-adjusted to match the rate of decay and magnitude of the voltage degradation. This iterative process allows all six tunable parameters to be identified.

3.1. Summary of modeling assumptions

In summary, the following general assumptions were made in developing the model presented:

- The volume of liquid water within the GDL does not restrict the volume occupied by the gases. The authors in Ref.

[36] indicated that the diffusion of gas through the GDL occurs through a hydrophobic macroporous structure, where as the liquid water travels through the non-wet proofed pores (a microporous structure), implying that the pore volume occupied by gases is fixed. Examining the time scale decomposition of the reactant and water dynamics [37], this assumption primarily influence the liquid water dynamics and due to the relatively small change in liquid water volume between the GDL sections, has a negligible impact. However, if different boundary conditions were applied which significantly modified the spatial distribution of liquid water in the GDL sections, this assumption should be revisited.

- The internal cell structure (gas channel, GDL and membrane) is assumed to be isothermal and equal to the time varying coolant outlet temperature. However, the gas inlet temperatures vary and are used to calculate the water vapor mass flow rates entrained with the supplied reactants. Although it is true that a multi-cell stack with a large active area will undoubtedly have thermal gradients within the cell structure and impact water transport [38], this assumption is adequate for estimating the temporal evolution in cell voltage experimentally observed under both flooding and drying conditions, as will be shown in Section 8. Accounting for dynamic thermal states within the gas diffusion layer adds a significant degree of model complexity which, while useful for design, may not be appropriate for control.
- The gas channels are treated as homogeneous and lumped parameter. Additionally, flow through the GDL is modeled in one dimension which neglects the difference in transport mechanisms for flow under the ribs versus under the channels. Although models do exist which characterize all these complex phenomena, the inclusion of this additional dimension has a significant impact on the number of internal states in the model.
- The only mechanism for removing liquid water from the gas channels is through evaporation. Although this is a common modeling assumption, it could result in an underestimation of the total mass of water (liquid and vapor) removed from the anode during purges. The tuned model parameters may compensate for this underestimation but the identified values were physically reasonable and within ranges reported in literature as discussed in Section 6. It has been shown [39] that liquid water droplet instability and the resultant detachment from the GDL to the gas channel can be a significant liquid water removal mechanism at high current density (high gas velocity). Therefore, if this model is to be extended to high current density operation, this assumption should be revisited.
- All gases behave ideally. The range of system operating temperatures and pressures permits the assumption of ideal gas behavior for the gas constituents of interest.
- Hydrogen, oxygen and nitrogen molecules do not crossover through the membrane. Although these thin polymeric membranes permit the crossover of molecules when there is a concentration gradient across the membrane [40], only the water crossover at steady-state has been considered in this work for the sake of model simplicity.
- Due to the relatively small gas flux within the GDL at the current density range considered, the convective transport of gas due to bulk flow was neglected.

3.2. Nomenclature

This section describes the nomenclature used throughout this paper. A list of the parameters is provided in Appendix A, along with values and units. Time derivatives are denoted as $\mathrm{d}(\,)/\mathrm{d}t$. Spatial derivatives through the GDL thickness in the membrane direction (y) are denoted as $\partial(\,)/\partial y$. In the presented model, all equations have SI units of Pa, N, m, kg, s, and J unless explicitly stated.

The symbol a is used for water activity, c for molar concentration (mol $\mathrm{m}^{(-3)}$), $\langle D\rangle$ for effective diffusivity ($\mathrm{m}^2\,\mathrm{s}^{-1}$), D_w for water vapor diffusion coefficient ($\mathrm{m}^2\,\mathrm{s}^{-1}$), E for the theoretical open circuit voltage (V), i for the nominal current density ($\mathrm{A\,cm}^{-2}$), i_app for the apparent current density ($\mathrm{A\,cm}^{-2}$), i_0 for the exchange current density ($\mathrm{A\,cm}^{-2}$), I for the total stack current (A), K_rl for relative permeability, n_d for electroosmotic drag coefficient (mol H_2O/mol H^+), N for molar flux (mol $\mathrm{s}^{-1}\,\mathrm{m}^{-2}$), p for pressure (Pa), p_sat for the water vapor saturation pressure (Pa), R_evap for the evaporation rate (mol $\mathrm{s}^{-1}\,\mathrm{m}^{-3}$), s for the fraction of liquid water volume to the total volume, S for the reduced liquid water saturation, T for temperature (K), U_act for the activation voltage loss (V), U_ohmic for the ohmic voltage loss (V), U_conc for the concentration voltage loss (V), $\bar{v}$ for the measured terminal cell voltage (V), $\hat{v}$ for the estimated terminal cell voltage (V), W for mass flow rate (kg s^{-1}), x for the mass fraction, and y for the mole ratio. Greek letters are used where ε is for the GDL porosity, λ for membrane water content (mol H_2O/mol SO_3^-), ϕ for relative humidity (0–1), and ω for humidity ratio.

The subscript amb is used to represent ambient conditions, an for anode, c for capillary, ca for cathode, ch for channel, ct for catalyst, da for dry air, dg for dry gas, e for electrode (an or ca), fc for fuel cell stack, H_2 for hydrogen, in for the control volume inlet or input, j as an index for gas constituents, k as an index for discretization (in time or space), l for liquid water, mb for membrane, N_2 for nitrogen, O_2 for oxygen, out for the control volume outlet or output, p for pore, rm for return manifold, v for water vapor, and w for water (gas and/or liquid phase).

3.3. Liquid water capillary transport

In hydrophobic GDL material, as the GDL pore spaces fill with liquid water, the capillary pressure increases, causing the water to flow to adjacent pores with less water. This process creates a flow of liquid water through the GDL, resulting in an injection of liquid into the channel. Applying the conservation of mass to the GDL volume, the liquid water dynamics, which arise from capillary liquid water mass flow, W_l, and the molar evaporation rate, R_evap, can be calculated by

$$\frac{\mathrm{d}s}{\mathrm{d}t} = \left(\frac{1}{\rho_\mathrm{l}\varepsilon A_\mathrm{fc}}\right)\frac{\partial W_\mathrm{l}}{\partial y} - \frac{R_\mathrm{evap}M_\mathrm{v}}{\rho_\mathrm{l}} \tag{1}$$

where the mass of liquid water in the GDL is expressed in terms of liquid water saturation, s, which represents the fraction of the liquid volume to the pore volume ($s = V_l/V_p$), A_{fc} the nominal fuel cell active area, ρ_l the liquid water density, M_v the molecular weight of water, and ε is the GDL porosity.

The flow of liquid water through the GDL is a function of the capillary pressure gradient [41,42] described by

$$W_l = -\frac{\varepsilon A_{fc}\rho_l K K_{rl}}{\mu_l}\left(\frac{\partial p_c}{\partial S}\right)\left(\frac{\partial S}{\partial y}\right), \tag{2}$$

where p_c is the liquid water capillary pressure, K the absolute permeability, μ_l the viscosity of liquid water, and $K_{rl} = S^3$ is the relative permeability of liquid water. The relative permeability function suggests more pathways for capillary flow are available as liquid water saturation increases, and is a function of the reduced liquid water saturation, S, shown by

$$S = \begin{cases} \dfrac{s - s_{im}}{1 - s_{im}} & \text{for } s_{im} < s \le 1 \\ 0 & \text{for } 0 \le s \le s_{im}, \end{cases} \tag{3}$$

where s_{im} is the value of the immobile saturation describing the point at which the liquid water path becomes discontinuous and interrupts capillary flow. This capillary flow interruption occurs when $s < s_{im}$. The results of capillary flow experiments using glass beads as porous media show that $s_{im} = 0.1$ [41].

Capillary pressure is the surface tension of the water droplet integrated over the surface area. The Leverett J-function describes the relationship between capillary pressure and the reduced water saturation, S,

$$p_c = \frac{\sigma \cos\theta_c}{\sqrt{K/\varepsilon}}\underbrace{[1.417S - 2.120S^2 + 1.263S^3]}_{J(S)}, \tag{4}$$

where σ is the surface tension between water and air, and θ_c is the contact angle of the water droplet [41].

Finally, the molar evaporation rate is

$$R_{evap} = \gamma\frac{p_{sat} - p_v}{RT}, \tag{5}$$

where γ is the volumetric condensation coefficient [41], R the ideal gas constant, T the temperature, p_{sat} the water vapor saturation pressure which itself is a function of temperature, and p_v is the water vapor partial pressure. When the partial pressure of water vapor is greater than the saturation pressure, R_{evap} is negative, representing the condensation of water. A logical constraint must be included such that if no liquid water is present ($s \le 0$) and the saturation pressure is greater than the water vapor pressure, then water can not be evaporated ($R_{evap} = 0$).

3.4. Gas species diffusion

The diffusion of gas species in the GDL is a function of the concentration gradient, transferring gas from regions of higher concentration to regions of lower concentration. The molar concentration of gas species j is denoted c_j and is a function of the number of moles of gas within the pore volume, V_p, where

$$c_j = \frac{p_j}{RT}. \tag{6}$$

Diffusion of hydrogen and water vapor occurs in the anode GDL and the diffusion of oxygen and water vapor occurs in the cathode GDL. As a result, both the anode and cathode gas diffusion can be modeled assuming binary diffusion. It is important to note that nitrogen gas is present in the cathode. As a result, the nitrogen concentration in the channel is calculated and assumed to the constant through the GDL since it is not involved in the reduction reaction at the catalyst. Ternary diffusion must be assumed at both the anode and the cathode if nitrogen cross-over were to be considered. The total molar flux is related to the concentration gradient, represented by

$$N_j = -\langle D_j\rangle\frac{\partial c_j}{\partial y}, \tag{7}$$

where $\langle D_j\rangle$ is the effective diffusivity of the gas constituents in the GDL,

$$\langle D_j\rangle = D_j\varepsilon\left(\frac{\varepsilon - 0.11}{1 - 0.11}\right)^{0.785}(1 - s)^2, \tag{8}$$

for two-dimensional bulk diffusion with flow perpendicular to the GDL carbon fibers, where D_j is the gas diffusion coefficient. Porosity, effective diffusivity and liquid water saturation for carbon Toray® paper GDL, are modeled from [41].

Finally, the general temporal derivative of gas concentration as a function of the local molar flux gradient and the local reaction rate, R_j, of the particular gas species forms a partial differential equation (PDE),

$$\frac{dc_j}{dt} = \frac{\partial N_j}{\partial y} + R_j \tag{9}$$

where (7)–(9) are combined to yield a second order PDE.

4. Boundary conditions

The membrane and gas channels serve as time-varying boundary conditions for the GDL model. This section presents the application of mass conservation in the channel as well as the model for the water vapor exchange between the anode and cathode through the membrane. It is important to remember that the spatial gradients within the GDL are approximated with finite difference equations. A variable taken from a GDL section that is adjacent to the boundary of interest will be denoted by $\psi(1)$ or $\psi(L)$, where ($L = 3$) indicates the section next to the gas channel and (1) indicates the section next to the membrane.

Each gas diffusion layer is separated into ($L = 3$) discrete volumes, shown in Fig. 4, to approximate the solution of (1) and (9) for each of the constituents in the GDL. Spatial discretization of the GDL yields eighteen coupled ordinary differential equations (ODEs), describing the gas constituent concentrations and liquid water saturation, that approximate the solution of the original PDEs.

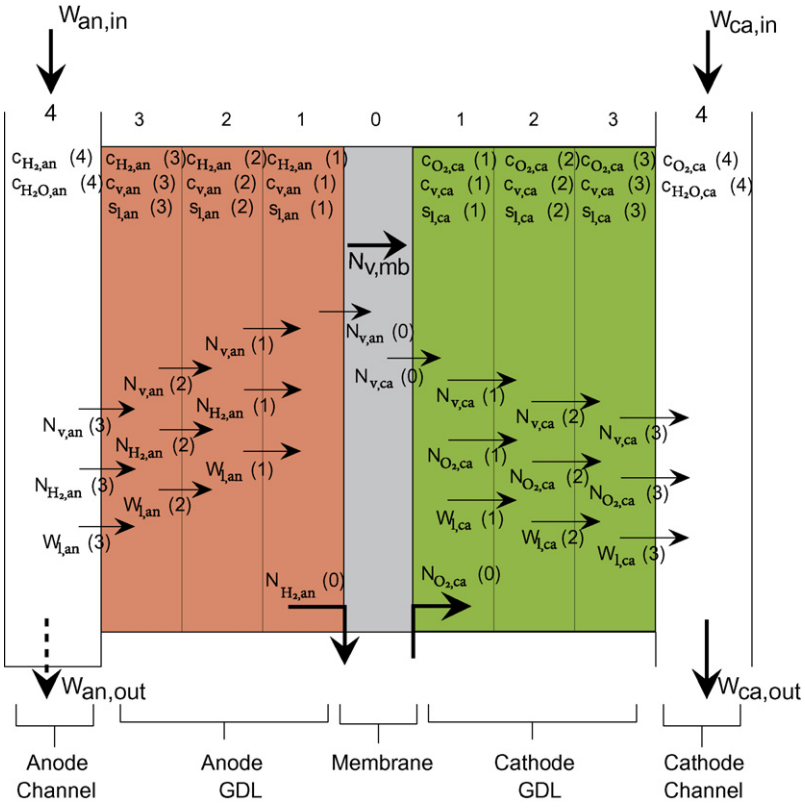

Fig. 4. Discretization of the gas diffusion layers. The direction of the assumed mass flow rate is indicated with a solid arrow. The dashed arrow is used to indicate periodic mass flow rates.

4.1. Membrane boundary conditions

The reaction at the catalyst surface of the membrane results in a loss of hydrogen and oxygen at the anode and cathode, respectively. These fluxes, $N_{j,e}(0)$, are used in the calculation of the molar flux spatial gradients, described by

$$N_{j,e}(0) = \frac{I}{\varepsilon A_{fc} 2\xi F} \text{with } \xi = \begin{cases} 1 & \text{for } j = H_2 \\ 2 & \text{for } j = O_2 \end{cases} \quad (10)$$

where I is the total current drawn from the stack and F is the Faraday constant. The molar flux of water vapor at the GDL–membrane boundary, $N_{v,e}(0)$, is influenced by the generation of water vapor at the cathode membrane surface as well as the flow of water vapor through the membrane, such that

$$N_{v,an}(0) = \frac{1}{\varepsilon} N_{v,mb}, \quad (11a)$$

$$N_{v,ca}(0) = \frac{1}{\varepsilon}\left(\frac{I}{2FA_{fc}} + N_{v,mb}\right). \quad (11b)$$

Note, a scaling factor of $1/\varepsilon$ is used here to ensure that the water vapor mass flow rate through the membrane is equal to the mass flow rate entering the GDL at the membrane boundary.

The water content of the membrane influences the membrane vapor transport which establishes a time-varying boundary condition for both the anode and the cathode. These membrane properties, described in Ref. [30], are assumed to be invariant across the membrane surface. The spatial variation of water vapor throughout the membrane is neglected due to the significant difference in thickness between the GDL (432 μm) and the membrane (35 μm). It is important to note that the membrane transport properties presented in this section are taken from experimental work conducted at steady-state. Non steady-state phenomena, such as membrane swelling and hysteresis, could be added in the future to improve model fidelity.

As with the other volumes, the membrane is considered to be homogeneous and lumped parameter. The flux of water vapor through the membrane, $N_{v,mb}$, accounts for the effects of both back-diffusion and electro-osmotic drag, suggested by Springer et al. [30],

$$N_{v,mb} = n_d \frac{i}{F} - \alpha_w D_w \frac{(c_{v,ca,mb} - c_{v,an,mb})}{t_{mb}}, \quad (12)$$

where i is the nominal fuel cell current density (I/A_{fc}), n_d the electro-osmotic drag coefficient, D_w the membrane water vapor diffusion coefficient, and t_{mb} is the membrane thickness. The parameter α_w is a tunable parameter that will be identified using experimental data. The convective water transport mechanisms suggested in Refs. [7,38,43] are neglected due to the relatively small water pressure gradients at these operating conditions.

The electro-osmotic drag coefficient, described by Springer et al. [30], is calculated using

$$n_d = \frac{2.5\lambda_{mb}}{22} \quad (13)$$

where the membrane water content, λ_{mb} is defined as the ratio of water molecules to the number of charge sites.

The water vapor concentration in the electrode at the membrane surface is

$$c_{v,e,mb} = \frac{\rho_{mb,dry}}{M_{mb,dry}}\lambda_e \tag{14}$$

where $\rho_{mb,dry}$ is the membrane dry density, $M_{mb,dry}$ is the membrane dry equivalent weight, and λ_e is the membrane water content at the surface of the membrane next to either the anode or cathode GDL.

The water vapor diffusion coefficient for a perflourinated ionomeric membrane, Nafion® 117, was determined at 25 ° C by Fuller [31] by applying a mass balance to determine the water vapor flux through the membrane, resulting in

$$D_w = 3.5 \times 10^{-6}\left(\frac{\lambda_{mb}}{14}\right)\exp\left[\frac{-2436}{T}\right]. \tag{15}$$

Two different cubic polynomials were presented by Springer et al. [30] and Hinatsu et al. [44] to relate water activity to membrane water content at 30 ° C and 80 °C, shown as

$$\lambda_j^{30\,^\circ C} = 0.043 + 17.81a_j - 39.85a_j^2 + 36.0a_j^3 \tag{16a}$$

$$\lambda_j^{80\,^\circ C} = 0.300 + 10.8a_j - 16.0a_j^2 + 14.1a_j^3 \tag{16b}$$

where a is the water activity and the subscript j is used here to distinguish between the anode or cathode membrane surface and within the membrane itself, $j \in \{an,ca,mb\}$. To estimate the water content at intermediate temperatures and sub-saturated conditions [45], suggested a linear interpolation between the two uptake isotherms shown in (16), such that

$$\lambda_j = (\lambda_j^{80\,^\circ C} - \lambda_j^{30\,^\circ C})\left(\frac{T-303}{353-303}\right) + \lambda_j^{30\,^\circ C}. \tag{17}$$

It is important to note that these two uptake isotherms are applicable only when water is in the vapor phase ($a_j \leq 1$).

In Ref. [30] it was shown that a membrane equilibrated with liquid water has a water content of $\lambda = 16.8$ at 80 °C, which differs from the water content when the membrane is equilibrated with a saturated vapor. It was further indicated that the water content is sensitive to temperature when equilibrated with liquid water, but assumed to be a linear relationship between [$\lambda = 14$, $a = 1$] and [$\lambda = 16.8$, $a = 3$] regardless of temperature, due to a lack of data regarding the membrane equilibration for water in both the liquid and vapor phase. Similarly, we assume a linear relationship between the membrane water content when equilibrated with water vapor, shown in (17) for $a_j = 1$, and the value of $\lambda = 16.8$ at $a = 3$ published by Springer et al. [30], such that

$$\lambda_j = \left(\frac{16.8 - \lambda_j^{a=1}}{3-1}\right)(a_j - 1) + \lambda_j^{a=1} \tag{18}$$

for $1 < a_j < 3$. Further experimental results from [46] and [44] provided data regarding the temperature sensitivity of the membrane water content equilibrated with liquid water. However, fitting this data points to a non-monotonic behavior of $\lambda = f(a)$, at some temperatures within the operating range of the PEMFC, during the transition between water in the vapor and liquid phases ($a = 1$), hence this relationship is not considered in this work.

Finally, the membrane water activity is assumed to be the average between the anode and cathode water activities (defined by the GDL sections closest to the membrane surface), described by

$$a_{mb} = \frac{a_{an}(1) + a_{ca}(1)}{2} \quad \text{and} \quad a_e(1) = \frac{p_{v,e}(1)}{p_{sat}} \tag{19}$$

where $p_{v,e}(1)$ is the water vapor pressure in the GDL layer next to the membrane, calculated using the water vapor concentrations.

Note here, it is assumed that reactant molecules do not transfer through the membrane between the anode and the cathode. Additionally, only water vapor can penetrate the membrane, not liquid water, implying $W_{l,e}(0) = 0$.

In summary, the water vapor partial pressures in the GDL section closest to the membrane surfaces are used to determine the water activity in the first GDL section, which is assumed to be equal to the membrane water activity at the membrane–GDL interface. These two membrane water activities are averaged to calculate the lumped membrane water activity, which influence diffusion and electro-osmotic drag. Finally, the net water vapor flux is calculated, given diffusion, drag and the water vapor concentrations at the membrane surfaces.

4.2. Boundary conditions at the cathode channel

The concentration of oxygen and water vapor in the cathode channels, $c_{O_2,ca}(L+1)$ and $c_{v,ca}(L+1)$, are used for the calculation of the gas concentration gradient for the GDL section next to the channels, $(\partial c_{j,ca}/\partial y)(L)$. Mass conservation for the gas species in the cathode is applied using the cathode inlet conditions as inputs, requiring measurements of the dry air mass flow rate, $W_{da,ca,in}$, temperature, $T_{ca,in}$, total gas pressure, $p_{ca,in}$, and humidity, $\phi_{ca,in}$, along with the cathode outlet pressure, $p_{ca,out}$. After completing several experiments under a range mass flow rates and temperatures, it was found that the cathode inlet total gas flow was fully humidified and the cathode outlet total pressure was approximately atmospheric, motivating the assumptions that $\phi_{ca,in} = 1$ and $p_{ca,out} = p_{atm}$.

The mass flow rate of the individual gas species supplied to the cathode channel are calculated as follows:

$$W_{O_2,ca,in} = x_{O_2,ca,in}W_{da,ca,in}, \quad W_{N_2,ca,in} = x_{N_2,ca,in}W_{da,ca,in},$$
$$W_{v,ca,in} = \omega_{ca,in}W_{da,ca,in}, \tag{20}$$

where the humidity ratio, ω, is generally defined by

$$\omega = \frac{M_v}{M_{dg}}\frac{\phi p_{sat}}{p - \phi p_{sat}} \tag{21}$$

for a gas–water vapor mixture, with the mass fraction of oxygen and nitrogen in the dry air (da) defined as $x_{O_2} = y_{O_2}M_{O_2}/M_{da}$ and $x_{N_2} = (1 - y_{O_2})M_{N_2}/M_{da}$, where $M_{da} = y_{O_2}M_{O_2} + (1 - y_{O_2})M_{N_2}$ and y_{O_2} is the oxygen mole fraction in dry air.

The gas species mass in the cathode channel are balanced by applying mass continuity:

$$\frac{dm_{O_2,ca}(L+1)}{dt} = W_{O_2,ca,in} - W_{O_2,ca,out} + W_{O_2,ca}(L),$$
$$\frac{dm_{N_2,ca}(L+1)}{dt} = W_{N_2,ca,in} - W_{N_2,ca,out},$$
$$\frac{dm_{w,ca}(L+1)}{dt} = W_{v,ca,in} - W_{v,ca,out} + W_{w,ca}(L). \quad (22)$$

The cathode channel pressure is calculated applying Dalton's law such that

$$p_{ca}(L+1) = \underbrace{\frac{RT}{V_{ca}}\left(\frac{m_{O_2,ca}(L+1)}{M_{O_2}} + \frac{m_{N_2,ca}(L+1)}{M_{N_2}}\right)}_{p_{dg,ca}(L+1)} + \underbrace{\min\left[p_{sat}, \frac{RTm_{w,ca}(L+1)}{M_V V_{ca}}\right]}_{p_{v,ca}(L+1)}. \quad (23)$$

Although in the physical system the cathode air mass flow rate may be responsible for removing some liquid water from the cathode channel, for modeling purposes it is assumed that all water exiting the cathode is in the form of vapor.

The mass flow rate of gases exiting the cathode are calculated as

$$W_{ca,out} = k_{ca}(p_{ca}(L+1) - p_{ca,out}),$$
$$W_{da,ca,out} = \frac{1}{1+\omega_{ca,out}} W_{ca,out},$$
$$W_{O_2,ca,out} = x_{O_2,ca,ch} W_{da,ca,out},$$
$$W_{v,ca,out} = W_{ca,out} - W_{a,ca,out},$$
$$W_{N_2,ca,out} = (1 - x_{O_2,ca}) W_{da,ca,out}, \quad (24)$$

where k_{ca} is an orifice constant found experimentally. Although the mole fraction of oxygen at the cathode inlet is assumed to be constant, $y_{O_2,ca,in} = 0.21$, the mole fraction of oxygen in the channel (driving the outlet mass flow rates) is dependent upon the oxygen mass (pressure) state in the channel, such that $y_{O_2,ca} = p_{O_2,ca}/p_{ca}$.

Finally, the oxygen and total water mass flow rates between the GDL and the channel, $W_{O_2,ca}(L)$ and $W_{w,ca}(L)$, must be calculated to solve the mass conservation equations shown in (22). The oxygen mass flow through the GDL–channel interface is a function of the oxygen molar flux, $N_{O_2}(L)$. The total water mass flow rate, $W_{w,ca}(L)$, exchanged between the GDL and channel is a function of the liquid water mass flow, $W_{l,ca}(L)$, and the water vapor flux, $N_{v,ca}$. Both the oxygen and total water mass flow rates are described by

$$W_{O_2,ca}(L) = N_{O_2}(L) M_{O_2} \varepsilon A_{fc} n_{cells},$$
$$W_{w,ca}(L) = \left(W_{l,ca}(L) + N_{v,ca}(L) M_v \varepsilon A_{fc}\right) n_{cells}, \quad (25)$$

where the assumption $S_{ca}(L+1) = 0$ is employed in the calculation of the reduced water saturation gradient to determine the liquid water mass flow rate between the GDL–channel interface, $W_{l,ca}(L)$. Within the channel, the volume of liquid water is assumed to be negligible compared with the total channel volume, motivating this assumption that $S_{ca}(L+1) = 0$.

4.3. Boundary conditions at the anode channel

Similarly to the cathode, the inputs for the anode calculations are the measured anode inlet conditions including the dry hydrogen mass flow rate, $W_{H_2,an,in}$, the supply manifold temperature, $T_{an,in}$, the total pressure, $p_{an,in}$, and the relative humidity, $\phi_{an,in}$. Dry hydrogen is supplied to the anode, as a result $\phi_{an,in} = 0$. The resulting mass balances for hydrogen and water are

$$\frac{dm_{H_2,an}(L+1)}{dt} = W_{H_2,an,in} - W_{H_2,an,out} - W_{H_2,an}(L),$$
$$\frac{dm_{w,an}(L+1)}{dt} = W_{v,an,in} - W_{v,an,out} - W_{w,an}(L). \quad (26)$$

The dry hydrogen inlet mass flow rate, $W_{H_2,an,in} = k_{an,in}(p_{an,in} - p_{an}(L+1))$, is controlled with a pressure regulator to maintain a constant anode inlet total pressure. Because the hydrogen supplied to the anode is dry, the vapor mass flow rate is assumed to be zero ($W_{v,an,in} = 0$). In calculating the anode total channel pressure, both the partial pressures of hydrogen and water vapor must be estimated such that,

$$p_{an}(L+1) = \underbrace{\frac{RT}{M_{H_2} V_{an}} m_{H_2}(L+1)}_{p_{H_2,an}(L+1)} + \underbrace{\min\left[p_{sat}, \frac{RTm_{w,an}(L+1)}{M_v V_{an}}\right]}_{p_{v,an}(L+1)}. \quad (27)$$

The total mass flow rate leaving the anode channel, $W_{an,out}$, exists only during an anode gas purge to remove both water, and unfortunately, hydrogen. The equations quantifying the hydrogen and water vapor mass flow rates leaving the anode channel are expressed as

$$W_{an,out} = k_{an,out}(p_{an}(L+1) - p_{an,out}),$$
$$W_{H_2,an,out} = \frac{1}{1+\omega_{an,out}} W_{an,out},$$
$$W_{v,an,out} = W_{an,out} - W_{H_2,an,out}. \quad (28)$$

Similarly to the cathode, the gas and liquid water mass flow rates between the GDL and channel are calculated by

$$W_{H_2,an}(L) = N_{H_2}(L) M_{H_2} \varepsilon A_{fc} n_{cells},$$
$$W_{w,an}(L) = (W_{l,an}(L) + N_{v,an}(L) M_v \varepsilon A_{fc}) n_{cells} \quad (29)$$

where the assumption $S_{an}(L+1) = 0$ is employed in the calculation of the reduced water saturation gradient to determine the

liquid water mass flow rate between the GDL–channel interface, $W_{l,an}(L)$.

The calculation of the mass flow rates leaving the anode channel depends on the measurement of the anode outlet total pressure, $p_{an,out}$, shown in (28). The anode outlet pressure can also be estimated using a similar approach as presented for the anode channel and documented in Ref. [26], where $W_{an,rm} = k_{an,rm}(p_{an,out} - p_{amb})$, resulting in the addition of two states (hydrogen and water mass in the return manifold).

5. Output voltage equation

In this section, the voltage equation is presented as a mapping from the apparent current density, reactant concentrations, temperature and membrane humidity conditions. All units for current density used throughout the presentation of the voltage model are given in A cm^{-2} for consistency with other published models.

Once anode flooding occurs, we associate the resulting voltage degradation with the accumulation of liquid water mass in the anode channel,

$$m_{l,an}(L+1) = \max\left[0, m_{w,an}(L+1) - \frac{p_{sat} M_v V_{an}}{RT}\right], \quad (30)$$

where the mass of water in the anode channel, $m_{w,an}(L+1)$, is taken from (26). The accumulated liquid water mass is assumed to form a thin film of thickness, t_{wl}, blocking part of the active fuel cell area, A_{fc}, and consequently increasing the apparent current density [20]

$$i_{app}(\mathrm{A\,cm^{-2}}) = \frac{I(\mathrm{A})}{10,000 A_{app}(\mathrm{m^2})}, \quad (31)$$

where the apparent fuel cell area A_{app} is approximated as

$$A_{app} = A_{fc} - \frac{2 m_{l,an}(L+1)}{n_{cells}\,\rho_l\,t_{wl}}. \quad (32)$$

The scaling factor of 2 in (32) was used to account for the fact that one half of the surface area at the GDL–channel interface is occupied by channel ribs, which reduces the area available for the formation of a liquid water film. This methodology for relating the accumulation of the liquid water in the channel to a restricted active area was first proposed in Ref. [20] and a similar methodology was employed by Hernandez et al. [29]. Some models that deal with cathode flooding, however, propose an increased current density due to the water accumulation in the catalyst layer at the GDL–membrane interface [47]. Ongoing experimental work from many researchers has focused on quantifying this accumulation of liquid water using direct visualization [48] or neutron imaging techniques [3,6,49].

The thickness of this water layer, t_{wl} is a tunable parameter that impacts the rate at which the active area is reduced and in turn the rate of voltage decay as the liquid water accumulates. Note that the notion of apparent current density, influenced by t_{wl} in the gas channel, is a simplification of the flooding phenomena that nevertheless captures the experimentally observed dynamic voltage behavior of a multi-cell stack under a range of conditions including both flooding and non-flooding. As shown in Section 7, this tuned parameter is similar to that experimentally determined in Ref. [6].

Once the apparent current density is calculated it is used, together with the partial pressure of the reactants in the anode and cathode GDL sections next to the membrane, to determine the average cell voltage. The average cell voltage, v, is equal to the theoretical open circuit voltage, E, minus the activation, U_{act}, and ohmic, U_{ohmic}, losses such that

$$v = E - U_{act} - U_{ohmic}. \quad (33)$$

We have assumed that the concentration voltage loss due to a mass transport limitation at high current density is negligible as a result of our operation at relatively low current densities ($i < 0.4$ A cm^{-2}).

The theoretical open circuit voltage, if the chemical reaction was a reversible process, varies with respect to reactant partial pressures and temperature according to the change in Gibbs free energy and the Nernst equation [50],

$$E = -\left(\frac{\Delta H}{2F} - \frac{T\Delta S}{2F}\right) + \frac{RT}{2F}\ln\left(\frac{p_{H_2,an}(1)\sqrt{p_{O_2,ca}(1)}}{(p_0)^{1.5}}\right) \quad (34)$$

where ΔS and ΔH are the differences in entropy and enthalpy from standard state conditions, p_0 the standard pressure, and the oxygen and hydrogen partial pressures, $p_{O_2,ca}(1)$ and $p_{H_2,an}(1)$, are located in GDL Section 1 next to the membrane.

The activation overvoltage accounts for the energy required to drive the chemical reaction (a deviation from equilibrium), as well as the loss current density resulting from the transport of molecular hydrogen from the anode to the cathode through the membrane. The total activation voltage loss was parameterized according to [51], such that

$$U_{act} = K_1 \frac{RT}{F}\ln\left(\frac{i_{app} + i_{loss}}{i_0}\right), \quad (35)$$

where K_1 is a tunable parameter representing the reciprocal of the charge transfer coefficient, i_{loss} the loss current density due to hydrogen crossover, i_{app} the apparent current density that is a function of the reduced active area due to the accumulation of liquid water at the GDL–channel interface from (31), and i_0 is the exchange current density which is a function of the reactant partial pressure and temperature [51], expressed as

$$i_0 = K_2\left(\frac{p_{O_2,ca}(1)}{p_0}\right)^{K_3}\exp\left[-\frac{E_c}{RT}\left(1 - \frac{T}{T_0}\right)\right], \quad (36)$$

where K_2 and K_3 are tunable parameters, E_c the activation energy for oxygen reduction on Pt, and T_0 is the reference temperature.

The ohmic voltage loss is dominated by the membrane conductivity as well as the contact and bulk electrical resistance of the conductive materials. This loss was shown experimentally in Ref. [30] to have the following functional form,

$$U_{ohmic} = K_4\left[\frac{t_{mb}}{(b_{11}\lambda_{mb} - b_{12})}e^{-1268\left(\frac{1}{303} - \frac{1}{T}\right)}\right] i_{app}, \quad (37)$$

where K_4 is a tunable parameter, t_{mb} is the membrane thickness, b_{11} and b_{12} the experimentally identified parameters from [30], and λ_{mb} is the membrane water content from (16)–(18).

6. Parameter identification approach

Lacking a practical experimental means to measure the spatial distribution of water mass in the anode and cathode of a large multi-cell stack for the use of online control, the lumped-parameter two-phase flow model developed here is indirectly calibrated and validated through model prediction of the effects of flooding on cell voltage. A reasonably wide variation in the experimental operating conditions have been examined, including both flooding and non-flooding conditions, to ensure that the model adequately estimates the relationship between GDL flooding and cell voltage degradation. The range of operating conditions examined is limited due to our operation with a stack, not a single cell, and our desire to minimize cell to cell voltage variations [52].

There exists two sets of model parameters which must be either calibrated or tuned. The calibrated parameters are based on the fuel cell hardware specifications and are listed in Table 1 with values provided in Appendix A. These parameters may require additional experiments to determine, such as the orifice constants describing the back pressure flow characteristics for each gas channel.

The two water related tunable parameters that require experimental identification are the: scaled "stack-level" membrane back diffusion, α_w, of (12), and thickness of liquid water layer accumulating at the GDL–channel interface, t_{wl}, of (32). Additionally, there are four tunable parameters K_1– K_4 associated with the output voltage in (33)–(37). Although the water related parameters do not appear linearly, the voltage equation can be rearranged such that each of the tunable K's is linear in the coefficient,

$$\hat{v} = E - K_1\frac{RT}{F}\left(\ln(i_{app}+i_{loss}) + \frac{E_c}{R}\left(\frac{1}{T}-\frac{1}{T_0}\right)\right) \quad (38)$$

$$+\ln(K_2)K_1\frac{RT}{F} + K_3K_1\frac{RT}{F}\ln\left(\frac{p_{O_2,ca}(1)}{p_0}\right) \quad (39)$$

Table 1
Parameters required based on PEMFC stack specifications

A_{fc}	Fuel cell nominal active area
K	Absolute permeability
$M_{m,dry}$	Membrane dry equivalent weight
n	Number of cells in the stack
t_{gdl}	GDL thickness
t_{mb}	Membrane thickness
V_{an}	Total anode channel volume
V_{ca}	Total cathode channel volume
ϵ	GDL porosity
$\rho_{m,dry}$	Membrane dry density
k_{an}	Anode orifice constants
k_{ca}	Cathode orifice constants

Note: values for these parameters are provided in Appendix A.

$$-K_4\left[\frac{t_{mb}}{(b_{11}\lambda_{mb}-b_{12})}e^{-1268\left(\frac{1}{303}-\frac{1}{T}\right)}\right](i_{app}+i_{loss}). \quad (40)$$

Given a set of values for α_w and t_{wl}, the voltage parameters were identified using linear least squares to minimize the difference between the measured average cell voltage, $\bar{v}$, and the modeled cell voltage, $\hat{v}$,

$$J = \int^{t_{exp}} [\bar{v}(\tau)-\hat{v}(\tau)]^T[\bar{v}(\tau)-\hat{v}(\tau)]\,d\tau, \quad (41)$$

over the experimental testing time, t_{exp}. The statistics associated with the estimation error were examined over a range of $[\alpha_w, t_{wl}]$ pairs to find the locally optimal $[\alpha_w, t_{wl}]$ combination and the resulting K values.

Note here, there are 24 individual cell voltages being measured. The average and median cell voltages exhibit similar dynamics with a relatively small difference in voltage between them. However, there is a significant difference in the magnitude and deviation between the minimum and maximum cell voltages. As a result, the use of either the minimum or maximum cell voltages for parameter tuning results in an underestimation or overestimation of the degree of flooding. For these reasons, the average cell voltage is used for model tuning.

7. Model calibration

Experimental calibration data were collected for a range of nominal stack current densities from $i = 0$ to 300 mA cm^{-2}, air stoichiometries of 250% and 300%, and coolant outlet temperatures from 45 to 63 °C, at an anode inlet total pressure of 1.2 bar, as shown in Fig. 5. A polarization curve (I–V) was conducted at approximately 70 min, at which time the purge events were temporarily disabled.

The purge events were scheduled to occur every 180 s for a duration of 1 s. During purge events, the purge solenoid valve was momentarily opened, exposing the anode outlet manifold to ambient pressure. As a result of this decreased anode total pressure, the manual pressure regulator, which tries to maintain its downstream pressure, increased the hydrogen mass flow rate through the system. Following the closure of the purge solenoid valve, small spikes in pressure occur as the pressure regulator readjusted its delivery pressure.

As shown in Fig. 5, the initial coolant outlet temperature setpoint was 50 ° C and then changed to 60 ° C at approximately 185 min. Thermostatic controllers were used to control the heat exchanger fans to regulate the coolant outlet temperature. As these fans were cycled, oscillations in temperature were induced.

The standard deviation in the cell voltage measurements was greater at high current density (300 mA cm^{-2}) than at low current density [52]. This increased uncertainty at high current density, seen in Fig. 5, was due to both the increased difference in the cell to cell voltage variation as well as the increased excursions in cell voltage between anode purges. Moreover, at high current density the cell with the minimum voltage exhibited greater voltage excursions between anode purges than the

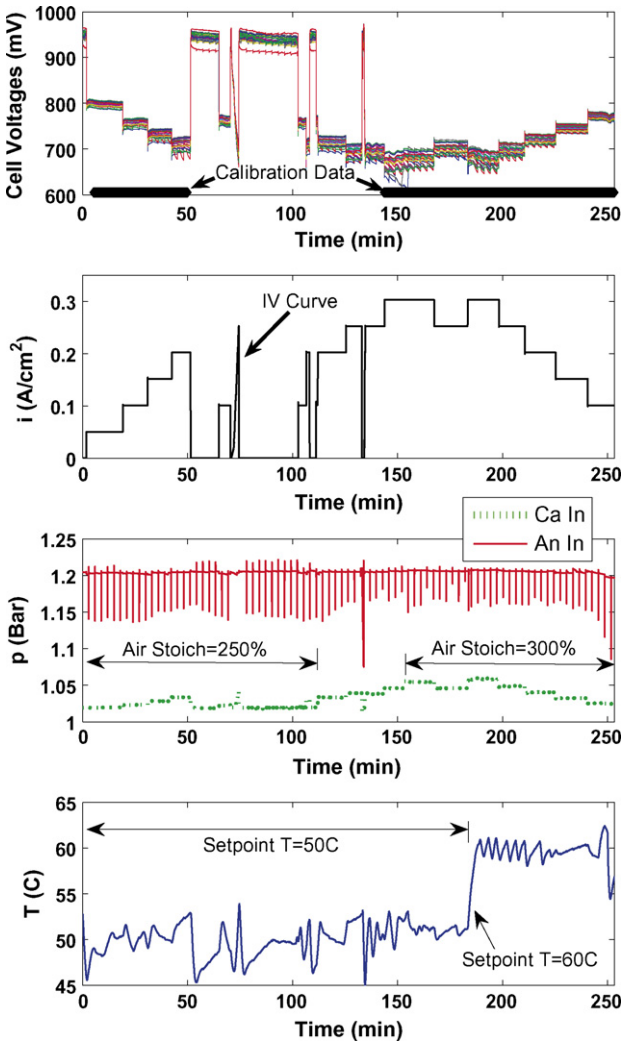

Fig. 5. Experimental measurements used for model calibration. The first subplot shows the 24 individual cell voltages along with black dots at 600 mV which illustrate the portions of the data set used for calibration. The second subplot shows the nominal current density. The third subplot is the anode and cathode inlet total pressures. The fourth subplot is the temperature of the water coolant leaving the stack.

cell with the maximum voltage. However, the mean and median voltages had similar dynamic and steady-state responses.

For the purposes of model calibration, a portion of the calibration data set was selected to include a range of both transient and "steady-state" operating conditions. This portion of data is indicated with a black x in the voltage plot shown in Fig. 5. Data at open-circuit were avoided due to the high uncertainty associated with operation at open-circuit voltage [52]. The identified parameters resulting in the smallest mean, maximum and standard deviation in the estimation error over the set of $\alpha_w \in [7, 12]$ and $t_{wl} \in [0.12\,\text{mm}, 0.14\,\text{mm}]$, while still capturing the voltage response during flooding conditions, are shown in Table 2.

The first tunable voltage parameter, K_1, which scales the total activation overvoltage has a local minimum, whose value is dependent on t_{wl}, near $\alpha_w = 10.5$. The second and third tunable voltage parameters, K_2 and K_3, influence the exchange current density and tend to increase as α_w increases or t_w decreases.

Table 2
Experimentally identified parameter values

Parameter	Tuned value
K_1	1.00
K_2 (μA)	1.24
K_3	2.05
K_4	3.40
α_w	10.0
t_{wl} (mm)	0.14

The fourth tunable voltage parameter, K_4, scales the ohmic overvoltage and decreases as α_w increases or t_w decreases.

Using the identified parameters, the model was simulated to produce voltage estimations for the entire calibration data set. Fig. 6 shows the model estimation at 300 mA cm^{-2} between 180 and 200 min. The second subplot compares the nominal

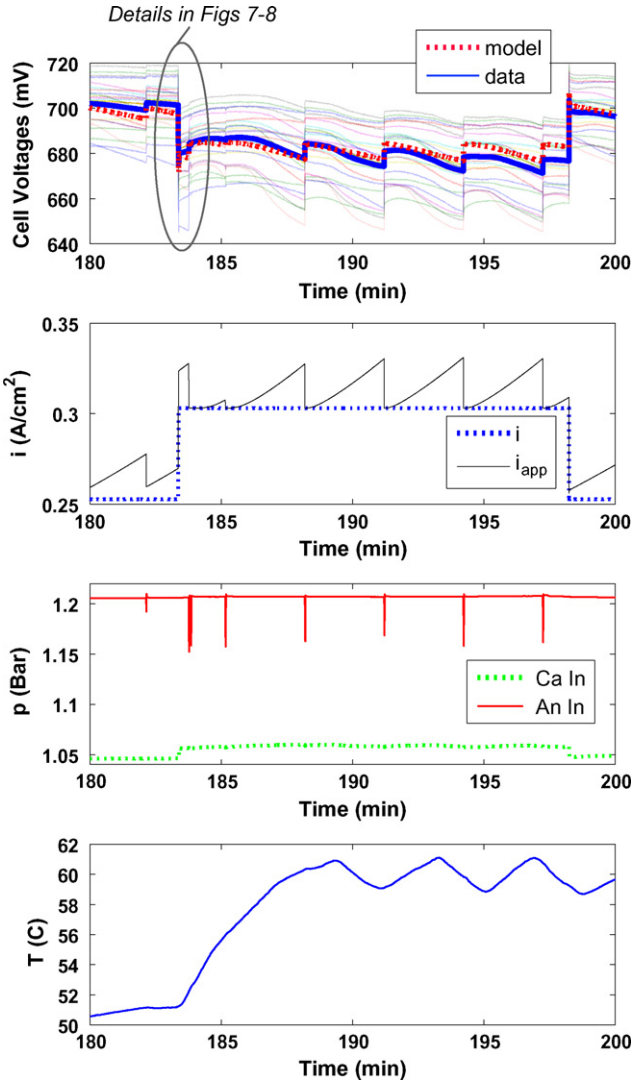

Fig. 6. Model calibration results. The first subplot shows the 24 individual cell voltages in thin faint colored lines with the average cell voltage in a thick solid blue line and the model estimated average cell voltage in a thick dotted red line. The second subplot shows the nominal and apparent current densities. The third subplot is the anode and cathode inlet total pressures. The fourth subplot is the temperature of the water coolant leaving the stack.

current density, $i = I/A_{fc}$, to the apparent current density, i_{app} from (31), based on the apparent surface area that is not blocked by the liquid water film at the GDL–channel interface.

As liquid water accumulated in the anode gas channels, the apparent area decreased, causing an increase in the apparent current density. Following a purge, the liquid water was removed and the apparent current density returned to the nominal value. Following some purges, not all of the water was removed from the gas channels, causing the apparent current density to remain greater than the nominal current density. Since the apparent current density was used to calculate the cell voltage, the estimation of cell voltage is then sensitive to the degree of flooding in the anode gas channels and GDL. The values for the identified parameters, α_w and t_{wl} influence the rate at which liquid water accumulates in the gas channels (impacting the rate of decay in voltage between purges) as well as how much liquid water mass accumulates in the gas channel (how much the voltage recovers following a purge). When all of the liquid water was removed from the gas channels, the cell voltage returned to approximately the same value following each purge event.

Although the voltage prediction is an indirect means for evaluating the overall predictive ability of our model, voltage is a stack variable that combines the internal states of the stack and provides an accessible, cheap, fast and accurate measurement. The model accurately captured the trend of the voltage decay and subsequent recovery after an anode purging event. Note here, for the entire calibration data set, the average estimation error was 2.9 mV, the maximum estimation error was 42 mV and the standard deviation in the estimation error was 3.6 mV.

In addition to adequately capturing the temporal evolution in voltage during flooding, the model accurately estimated the reactant dynamics during load changes. The overshoot in cell voltage during a step change up in current from 0.25 A cm^{-2} to 0.3 A cm^{-2} at approximately 183.4 min, is shown in detail in Fig. 7, along with subsequent purging events near 183.7 min. A decrease in the partial pressure of oxygen at the cathode membrane surface occurs due to volume filling dynamics; however, there was very little deviation in the hydrogen partial pressure during the load change. As a result, the reactant starvation occurred predominantly on the cathode and not the anode under these operating conditions. Referring back to Fig. 6, the overshoot in cell voltage at approximately 198 min for a step change down in current from 0.3 A cm^{-2}to 0.25 A cm^{-2}is also well approximated. Note here, for simulations of reactant dynamics during a load change reported in Refs. [23,53], the model predictions were not compared with experimental data.

Fig. 8 displays the predicted water vapor partial pressures, the liquid water saturation, and the mass of liquid water accumulating in the anode channel during the same load change and subsequent purging events as described previously for Fig. 7. The slow rise in the water vapor partial pressure was due to the increase in the cell operating temperature.

Immediately following the purge valve opening, the mass of liquid water in the anode channel was evaporated into the bulk gas stream (due to the increased hydrogen mass flow rate during the purge). The volumetric condensation coefficient, γ in (5), influenced the non-instantaneous rate of evaporation of

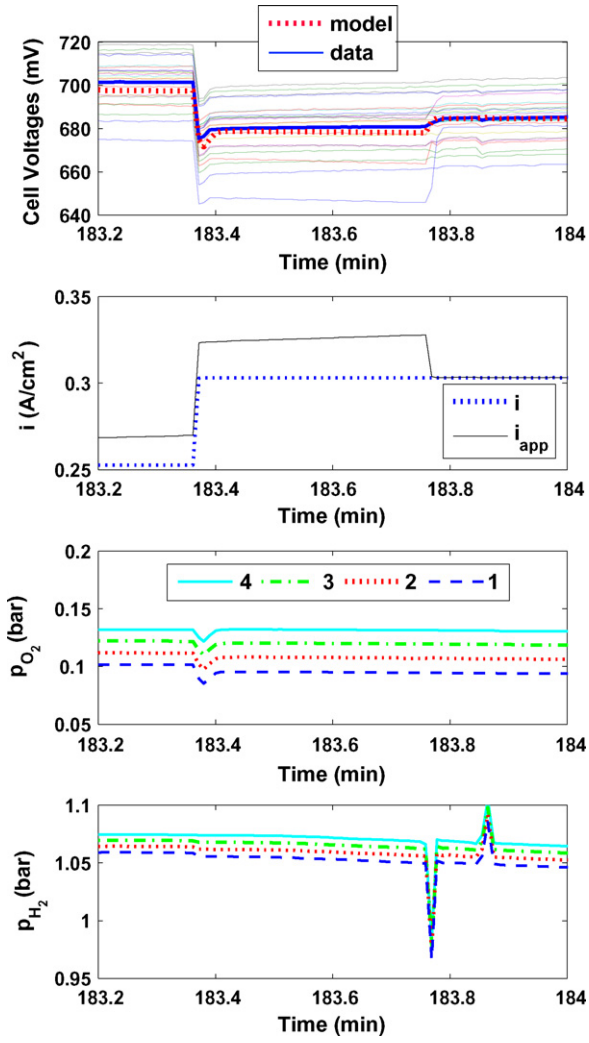

Fig. 7. Reactant dynamics during a load change and purging event. The first row of subplots shows the cell voltages along with the nominal and apparent current densities. The 24 individual cell voltages are displayed in thin faint colored lines with the average cell voltage based on the measurements in a thick solid blue line and the estimated cell voltage in a thick dotted red line. The second row of subplots show the oxygen and hydrogen partial pressures in each GDL Section (1–3) as well as in the channel (4). A load change from 0.25 A cm^{-2}to 0.3 A cm^{-2}occurs at approximately 183.4 min followed by an anode purging event at approximately 183.7 min

water vapor in the GDL section allowing the water vapor partial pressure to decrease before all of the liquid water was removed from the GDL sections.

The liquid water saturation in the GDL section closest to the channel, $s_{an}(3)$, decreased most significantly during a purge. Liquid water flowed from the GDL towards the channel until the immobile saturation limit was reached, $s_{an}(3) \leq s_{im}$, at which point only water vapor entered the channel from the GDL. Liquid water does not flow from the GDL to the anode channel, following the purge, until the liquid water saturation in the GDL exceeded the immobile saturation limit. If the purge event were to have occurred over a longer time interval, more water vapor in the anode GDL would have been removed, causing a more significant impact on the cathode liquid water saturation due to the water vapor transport through the membrane.

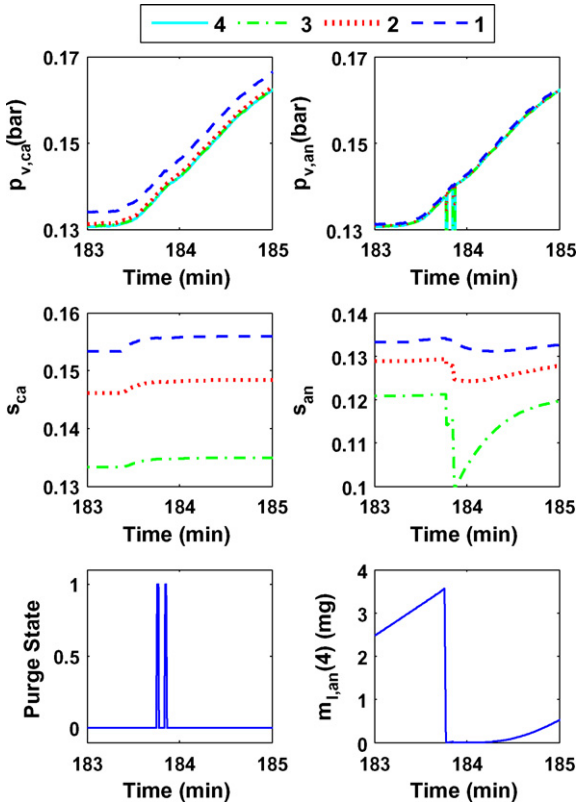

Fig. 8. Water dynamics during a load change and purging event. The first row of subplots shows the water vapor partial pressures in the GDL and channels. The channel is indicated by a solid line and the three GDL sections are represented by dashed lines. The second row of subplots displays the liquid water saturation in the GDL. Finally, the third row of subplots indicates first the state of the purge solenoid valve (0 indicates the valve is closed and 1 means the valve is open), followed by the mass of liquid water accumulating in the anode channel.

8. Model validation and discussion

For the purposes of model validation, the calibrated model was simulated with experimental inputs that were not considered in the calibration process. The resulting model predictions are shown in Fig. 9 and compared with the actual cell voltage measurements at five different load levels. The data shown demonstrates the model predicting capability over a range of current densities and air stoichiometries. At approximately 162 min, the air stoichiometry was increased from 200% to 300%, causing a more significant increase in the voltage estimation (through the partial pressure of oxygen at the membrane boundary) than was experimentally observed. Despite the increased error associated with the oxygen partial pressure, the model correctly estimated the degree of anode flooding at various current densities, correctly predicting no significant flooding at low loads. As the load level was reduced, the degree of flooding decreased, which is seen from inspection of the difference between the apparent and nominal current densities at each load level. As a result, the deviation in voltage decreased between purges, which was experimentally confirmed.

For the entire validation data set, the average estimation error was 8.7 mV, the maximum estimation error was 105 mV

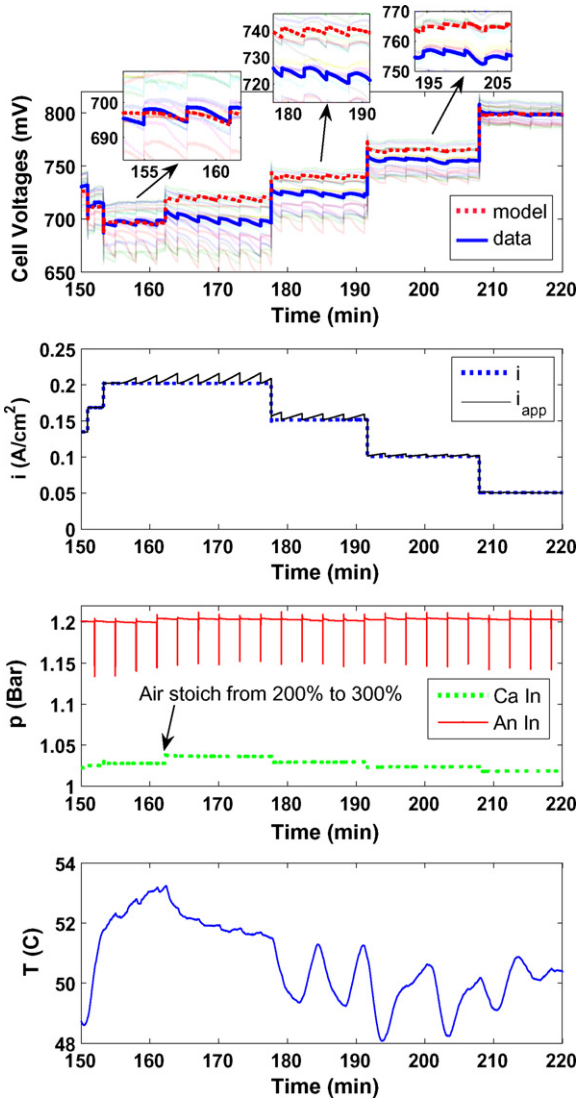

Fig. 9. Model validation results. The first subplot shows the 24 individual cell voltages in thin faint colored lines with the average cell voltage based on the measurements in a thick solid blue line and the estimated cell voltage in a thick dotted red line. The second subplot shows the nominal and apparent current densities. The third subplot contains the anode and cathode inlet total pressures. The fourth subplot is the temperature of the water coolant leaving the stack.

and the standard deviation in the estimation error was 11.5 mV. Although these validation error statistics are approximately two times greater than the error statistics associated with the calibration data, at all times throughout the experiment the estimated average cell voltage was bounded between the measured minimum and maximum cell voltages and the measured cell to cell variation was larger than the average estimation error.

Although the model of the reactant and water dynamics results in an accurate estimation of the voltage degradation between purges, we have made the assumption that this degradation was solely due to the accumulation of liquid water in the gas channels. However, it is conceivable that some of this degradation could be due to the accumulation of nitrogen on the anode as a result of operation with air, rather than pure oxygen, or catalyst flooding. Our model has tunable parameters that can

compensate for these model assumptions and simplifications, but it is very important to check the tuned parameter values against other published values. As Table 2 shows, the tuned α_w and t_{wl}, are reasonable and within the range of published results [6,27].

9. Conclusions

A two-phase isothermal one-dimensional model of reactant and water dynamics has been developed and validated using a multi-cell stack. The lumped parameter model depends on six tunable parameters associated with the estimation of voltage, the membrane water vapor transport and the accumulation of liquid water in the gas channels. During step changes in load, a good voltage prediction is achieved by reproducing both the steady-state and dynamic voltage response due to the instantaneous increase in current as well as the excursions in oxygen partial pressure resulting from the manifold filling dynamics, as demonstrated. Finally the model predicted the dynamic effect of temperature on voltage as shown during the temperature transient from 50° to 60 °C. Although simple, this model captures the voltage dynamics observed in a fuel cell stack at low and moderate current densities under the range of conditions tested. However, caution should be used in extending this model to conditions not examined, as the intent of this model is for control.

The notion of apparent current density is a means for describing the impact of water accumulation on the dynamic voltage behavior of a PEMFC. Future work is focused on extending and validating this simple GDL model at higher current density, and establishing the connection between the liquid water mass accumulation and voltage using neutron imaging techniques.

Acknowledgements

We gratefully acknowledge funding from the U.S. Army Center of Excellence for Automotive Research (DAAE07-98-3-0022), the National Science Foundation (CMS 0625610), and the U.S. Department of Energy (DE-FG02-06CH 11300).

Appendix A

The model parameters are listed in Table A.1 . It is important to note that for convenience the parameter values listed here may have units other than those expressed in the modeling equations.

Table A.1
Parameter symbols, definitions and values

Symbol	Definition
$A_{fc} = 0.030\,m^2$	Fuel cell nominal active area
$b_{11} = 0.005139$[30]	Ohmic resistance parameter
$b_{12} = 0.00326$[30]	Ohmic resistance parameter
$D_{H_2} = 114\,mm^2\,s^{-1}$ [41]	Hydrogen diffusion coefficient
$D_{O_2} = 30.3\,mm^2\,s^{-1}$ [41]	Oxygen diffusion coefficient
$E_c = 66\,kJ\,mol^{-1}$ [51]	Activation energy
$F = 96485\,C\,(mol\,e^-)^{(-1)}$	Faraday's constant
$\Delta H = -228,740\,J\,mol^{-1}$	Enthalpy difference from STP (water in vapor phase)
$i_{loss} = 1\,mA\,cm^{-2}$ [51]	Loss current density
$k_{ca,in} = 11.3E{-}7\,m\,s$	Cathode orifice constant
$k_{ca,out} = 11.3E{-}7\,m\,s$	Cathode orifice constant
$k_{an,in} = 9.34E{-}7\,m\,s$	Anode orifice constant
$k_{an,out} = 9.34E{-}7\,m\,s$	Anode orifice constant
$k_{an,rm} = 11.31E{-}7\,m\,s$	Return manifold orifice constant
$K = 2.55E{-}13\,m^2$ [41]	Absolute permeability
$K_1 = 1.17$	Tuned voltage parameter
$K_2 = 4.44\,\mu A$	Tuned voltage parameter
$K_3 = 1.78$	Tuned voltage parameter
$K_4 = 3.27$	Tuned voltage parameter
$L = 3$	Number of GDL sections
$M_{H_2} = 0.002\,kg\,mol^{-1}$	Hydrogen molecular weight
$M_{O_2} = 0.032\,kg\,mol^{-1}$	Oxygen molecular weight
$M_{N_2} = 0.028\,kg\,mol^{-1}$	Nitrogen molecular weight
$M_{H_2O} = 0.018\,kg\,mol^{-1}$	Water molecular weight
$n_{cells} = 24$ cells	Number of cells in stack
$p_0 = 1$ atm	Standard state pressure
$R = 8.314\,J\,mol^{-1}\,K^{-1}$	Universal gas constant
$s_{im} = 0.1$ [41]	Immobile saturation
$\Delta S = -44.43\,J\,mol^{-1}\,K^{-1}$	Entropy difference from STP (water in vapor phase)
$t_{gdl} = 0.5\,mm$	Total GDL thickness
$t_{mb} = 0.038\,mm$	PEMFC membrane thickness (includes catalyst layer)
$t_{wl} = 0.131\,mm$	Tunable water layer thickness
$T_0 = 298.15\,K$	Standard state temperature
$V_p = 2.5\,cm^3$	GDL section pore volume
$V_{ca} = 380\,cm^3$	Cathode channel volume
$V_{an} = 430\,cm^3$	Anode channel volume
$V_{an,rm} = 345\,cm^3$	Anode return manifold volume
$\alpha_w = 11.5$	Tuned water vapor diffusion parameter
$\delta y = 0.167\,mm$	GDL discretization width
$\gamma = 900\,s^{-1}$ [41]	Volumetric condensation coeff.
$\epsilon = 0.5$ [41]	Material porosity
$\theta_c = 60°$[41]	Contact angle
$\mu = 0.405\,g\,m^{-1}\,s^{-1}$ [41]	Liquid water viscosity
$\rho = 997\,kg\,m^{-3}$	Liquid water density
$\sigma = 0.0644\,N\,m^{-1}$ [41]	Surface tension
$\rho_{mb,dry} = 1900\,kg\,m^{-3}$	mb dry density
$M_{mb,dry} = 1.0\,kg\,mol^{-1}$	mb dry equivalent weight

References

[1] T. Zawodzinski, C. Derouin, S. Radzinski, R. Sherman, V. Smith, T. Springer, S. Gottesfeld, J. Electrochem. Soc. 140 (1993).
[2] M. Hickner, N. Siegel, K. Chen, D. McBrayer, D. Hussey, D. Jacobson, M. Arif, J. Electrochem. Soc. 153 (2006) A902.
[3] T. Trabold, J. Owejan, D. Jacobsen, M. Arif, P. Huffman, Int. J. Heat Mass Transfer 49 (2006) 4712.
[4] N. Pekula, K. Heller, P. Chuang, A. Turhan, M. Mench, J. Brenizer, K. Unlu, Proceedings of the Fifth International Topical Meeting on Neutron Radiography, vol. 542, 2005, p. 134.
[5] J. Zhang, D. Kramer, R. Shimoi, Y. Ono, E. Lehmann, A. Wokaun, K. Shinohara, G. Scherer, Electrochim. Acta 51 (2006) 2715.
[6] P.-Y.A. Chuang, A. Turhan, A.K. Heller, J.S. Brenizer, T.A. Trabold, M. Mench, in: Proceedings of the ASME Second International Conference on Fuel Cell Science, Engineering and Technology, 2005.
[7] J. Yi, T. Nguyen, J. Electrochem. Soc. 145 (1998).
[8] T. Fuller, J. Newman, J. Electrochem. Soc. 140 (1993).

[9] S. Dutta, S. Shimpalee, J.V. Zee, Int. J. Heat Mass Transfer 44 (2001) 2029.
[10] U. Pasaogullari, C. Wang, J. Electrochem. Soc. 152 (2005).
[11] L. You, H. Liu, Int. J. Heat Mass Transfer 45 (2002) 2277.
[12] T. Berning, N. Djilali, J. Electrochem. Soc. 150 (2003) A1589.
[13] Q. Guo, V. Sethuraman, R. White, J. Electrochem. Soc. 151 (2004) A983.
[14] B. Carnes, N. Djilali, J. Power Sources 144 (2005) 83.
[15] G. Suares, K. Kosanovich, Ind. Eng. Chem. Res. 36 (1997) 4264.
[16] G. Suares, K. Hoo, Chem. Eng. Sci. 55 (2000) 2237.
[17] H. Ju, C. Wang, J. Electrochem. Soc. 151 (2004) A1954.
[18] P. Berg, K. Promislow, J.S. Pierre, J. Stumper, B. Wetton, J. Electrochem. Soc. 151 (2004).
[19] D. Natarajan, T.V. Nguyen, AIChE J. 51 (2005) 2587.
[20] D.A. McKay, W.T. Ott, A. Stefanopoulou, in: Proceedings of the 2005 ASME International Mechanical Engineering Congress & Exposition, vol. IMECE 2005-81484, 2005.
[21] D. Natarajan, T.V. Nguyen, J. Electrochem. Soc. 148 (2001) A1324.
[22] Y. Wang, C. Wang, Electrochim. Acta 50 (2005) 1307.
[23] Y. Wang, C. Wang, Electrochim. Acta 51 (2006) 3924.
[24] Y. Shan, S.-Y. Choe, S.-H. Choi, J. Power Sources 165 (2007) 196.
[25] S. Shimpalee, D. Spuckler, J.V. Zee, J. Power Sources 167 (2007) 130.
[26] J. Pukrushpan, H. Peng, A. Stefanopoulou, J. Dyn. Syst. Meas. Control 126 (2004) 14.
[27] P.H. Rodatz, Ph.D. Thesis, Swiss Federal Institute of Technology, ETH, 2003.
[28] A.J. del Real, A. Arce, C. Bordons, J. Power Sources 173 (2007) 310–324.
[29] A. Hernandez, D. Hissel, R. Outbib, Fuel Cells (2005) 38–46.
[30] T. Springer, T. Zawodzinski, S. Gottesfeld, J. Electrochem. Soc. 138 (1991).
[31] T.F. Fuller, Ph.D. Thesis, University of California, Berkeley, 1992.
[32] S. Motupally, A. Becker, J. Weidner, J. Electrochem. Soc. 147 (2000).
[33] H. Yamada, Y. Morimoto, Res. Dev. Rev. Toyota CRDL 39 (2004).
[34] H. Ju, C. Wang, S. Cleghorn, U. Beuscher, J. Electrochem. Soc. 152 (2005) A1645.
[35] G. Lin, W. He, T.V. Nguyen, J. Electrochem. Soc. 151 (2004) A1999.
[36] J. Amphlett, R. Baumert, R. Mann, B. Peppley, P. Roberge, J. Electrochem. Soc. 142 (1995).
[37] B. McCain, A. Stefanopoulou, in: Proceedings of Fourth International Conference on Fuel Cell Science, Engineering and Technology, vol. FUELCELL2006-97075, 2006.
[38] N. Djilali, D. Lu, Int. J. Thermal Sci. 41 (2002) 29.
[39] E. Kumbur, K. Sharp, M. Mench, J. Power Sources 161 (2006) 333.
[40] S. Kocha, J. Yang, J. Yi, AIChE 52 (2006) 1916.
[41] J. Nam, M. Kaviany, Int. J. Heat Mass Transfer 46 (2003) 4595.
[42] M. Kaviany, Principles of Heat Transfer in Porous Media, Springer, New York, 1999.
[43] P. Costamagna, Chem. Eng. Sci. 56 (2001) 323.
[44] J. Hinatsu, M. Mizuhata, H. Takenaka, J. Electrochem. Soc. 141 (1994) 1493.
[45] K. Dannenberg, P. Ekdunge, G. Lindbergh, J. Appl. Electrochem. 30 (2000) 1377.
[46] T. Zawodzinski, T. Springer, F. Uribe, S. Gottesfeld, Solid State Ionics 60 (1993).
[47] Y. Wang, C. Wang, J. Electrochem. Soc. 154 (2007) B636.
[48] S. Litster, D. Sinton, N. Djilali, J. Power Sources 154 (2006) 95.
[49] D. Kramer, J. Zhang, R. Shimoi, E. Lehmann, A. Wokaun, K. Shinohara, G. Scherer, Electrochim. Acta 50 (2005) 2603.
[50] R.P. O'Hayre, S.-W. Cha, W. Colella, F.B. Prinz, Fuel Cell Fundamentals, Wiley, Hoboken, NJ, 2006.
[51] F. Barbir, PEM Fuel Cells: Theory and Practice, Elsevier, Burlington, MA, 2005.
[52] A. Schilter, D. McKay, A. Stefanopoulou, in: Proceedings of the ASME Fourth International Conference on Fuel Cell Science, Engineering and Technology, vol. FUELCELL2006-97177, 2006.
[53] J. Pukrushpan, A. Stefanopoulou, H. Peng, IEEE Control Syst. Mag. 24 (2004) 30.